A Single-Objective Modulated Model Predictive Control for a Multilevel Flying-Capacitor Converter in a DC Microgrid

Vijesh Jayan, *Student Member, IEEE*, and Amer Mohammad Yusuf Mohammad Ghias, *Senior Member, IEEE*

***Abstract*—This article presents a single-objective modulated model predictive control for a bidirectional dc–dc flying-capacitor (FC) converter in a microgrid. The presence of an FC facilitates the converter to integrate a low-voltage battery to a high-voltage dc bus at reduced voltage stress on its power switches. The converter in such a configuration demands a multiobjective controller to accomplish dc bus and FC voltage regulations and bidirectional power flow. The proposed controller realizes these multiple control objectives by determining the optimum duty ratio for the power switches using a single-objective cost function based on the battery current. In doing so, the converter realizes its multiple control objectives without weighting factors in the cost function and operates its power switches at a fixed switching frequency. The proposed controller also eliminates an additional control loop by utilizing an improved dynamic reference model to generate an appropriate battery current reference for the dc bus voltage regulation and bidirectional power flow. Finally, the proposed system is validated experimentally under step response of the dc bus voltage, load, PV power, and system parameter variations, and compared with a finite control set model predictive control to prove its effectiveness.**

***Index Terms*—Bidirectional dc–dc flying-capacitor (FC) converter, dc microgrid, fixed switching frequency, modulated model predictive control, weighting factor elimination.**

I. Introduction

THE rising environmental concerns on global warming and limited fossil fuel supplies have made mankind move toward the use of renewable energy source (RES) for power generation. However, the intermittent nature of RES introduces various risk during its integration to a dc bus [1]. To compensate this intermittency, energy storage device (ESD) such as battery is integrated to the dc bus through a bidirectional dc–dc converter [2]. The converter's main objective is to regulate the dc bus voltage by absorbing/supplying power from the ESD. Conventionally, these objectives were realized by a two-level bidirectional dc–dc converter that was controlled by two linear controllers connected in cascade configuration [3]–[6]. The ESD current control loop (inner loop) applied an appropriate switching signal to the converter based on the ESD current reference generated by the dc bus voltage control loop (outer loop). Despite its simple structure, such converter is not suitable for integrating low-voltage ESD to a high-voltage dc bus. This is because, the converter requires a large input filter and its power switches/diodes experience huge voltage stress during high voltage-gain operation [7]. In addition, the power diodes encounter a reverse-recovery issue due to extreme duty ratio operation leading to electromagnetic interference and efficiency reduction [8], [9]. Therefore, multilevel dc–dc converter emerged to facilitate a high voltage-gain conversion at improved efficiency, reduced voltage stress on the power switches/diodes, and reduced filter size requirement [10]. A dc microgrid application of a three-level bidirectional dc–dc converter based on neutral point (NP) and flying-capacitor (FC) was reported in [11] and [12], respectively. Besides the ESD current and dc bus voltage control loops, such converter also required an additional linear controller for its NP or FC voltage regulation. This made the overall control structure complicated and required tuning of their controller gains. Besides these complexities, a linear controller possesses a poor dynamic response as its gains are designed for a specific operating point. This can introduce an undesirable deviation in the system variables during disturbances such as fluctuating RES power injection and varying loads in a microgrid [13]. Thus, a dynamic multiobjective controller is required with easy implementation and capable of handling instantaneous RES power and load variations in a microgrid.

For the past few years, an increase in the use of finite control set model predictive control (FCS-MPC) for various industrial applications was reported [14]. Compared to the linear controller, the FCS-MPC have better dynamic response over a wide operating range and is capable of handling instantaneous power variations in a microgrid. Moreover, the FCS-MPC realizes multiple control objectives by including the control variables in the cost function with suitable weighting factors [15]. The FCS-MPC implementation of a three-level bidirectional dc–dc FC converter integrating the ESD to a dc bus was reported in [16]. An optimum state was applied to the converter by minimizing a multiobjective cost function based on the ESD

Manuscript received March 16, 2021; revised June 20, 2021 and August 15, 2021; accepted August 25, 2021. Date of publication September 1, 2021; date of current version October 15, 2021. This work was supported by the School of Electrical, and Electronic Engineering, Nanyang Technological University, Ministry of Education, Singapore, under Grant AcRF TIER 1-2018-T1-002-109 (RG 171/18). Recommended for publication by Associate Editor H. S. Krishnamoorthy. *(Corresponding authors: Vijesh Jayan and Amer M. Y. M. Ghias.)*

The authors are with the School of Electrical and Electronic Engineering, Nanyang Technological University, Singapore 639798, Singapore (e-mail: vijeshja001@e.ntu.edu.sg; amer.ghias@ntu.edu.sg).

Color versions of one or more figures in this article are available at https://doi.org/10.1109/TPEL.2021.3109048.

Digital Object Identifier 10.1109/TPEL.2021.3109048

current and FC voltage. However, a linear controller was utilized as a secondary control loop to generate ESD current reference for the dc bus voltage regulation. This worsened the converter dynamics and complicated the gain tuning procedure due to variable switching frequency. Another FCS-MPC implementation of a bidirectional dc–dc FC converter for dc microgrid application was reported in [17] and [18]. Instead of a linear controller, a dynamic reference model [19] was utilized to generate the ESD current reference for the dc bus voltage regulation. The model could easily control the dc bus voltage dynamics by adjusting a limiting parameter. As a result, the dc bus voltage regulation was realized without any additional control loop. Despite its dynamic performance, the converter's power switches were observed to operate at a variable switching frequency. This resulted in a huge current ripple, which increased the system losses and overstressed the ESD. Thus, a modulated MPC (MMPC) was developed in [20], where a valid optimum sequence of states was applied to the converter using a PS-PWM modulator to ensure a fixed switching frequency operation.

The MMPC implementation of a bidirectional dc–dc FC converter for a dc microgrid application was reported in [21] and [22]. The optimum duty ratio for the power switches were obtained by minimizing a multiobjective cost function based on the ESD current and FC voltages. The optimum sequence of states was applied to the converter by a PS-PWM modulator, which enabled it to realize the control objectives with a fixed switching frequency operation. However, the implementation required multiple iterations to determine the optimum duty ratio for each power switch. This made the approach complicated and computationally intensive. Moreover, the dc bus voltage was observed to have a steady-state error that was proportional to the limiting parameter used in the dynamic reference model. A continuous control set MPC implementation of a three-level FC boost converter was reported in [23], where an explicit expression for the optimum duty ratio of each power switch was derived. In doing so, the computational burden was reduced significantly as the optimum duty ratios were obtained without any iteration. However, these expressions had numerous predefined coefficients with complex mathematical formulations. The converter's performance was sensitive to these coefficients and required proper guidelines for its estimation. Thus, making the entire implementation complicated for the converter with higher levels. Besides these drawbacks, the aforementioned MPC implementations have weighting factors in their cost function that requires estimation. An inappropriate selection of these factors can cause a detrimental effect on the converter's dynamic performance [24].

The weighting factor estimation is nontrivial and one of the ongoing research challenges in FCS-MPC [25]. Several methods, namely the mean square error [26], the dynamic optimization [27], and the artificial neural network [28], were reported for weighting factor estimation. However, all these methods obtained appropriate weighting factor by running numerous simulations/experiments on a specific model with predefined parameters. This made the whole estimation process complicated and did not guarantee the desired performance for systems with different model parameters. Besides estimation, weighting factor elimination from the cost function was reported in [29] and [30]. These methods were easy to implement as the aforementioned complex analysis/numerical models were not required. However, such method drove the power switches at a variable switching frequency. The MMPC implementation of a bidirectional dc-dc NP converter without a weighting factor for a hybrid energy storage system was reported in [31]. The controller determined the optimum duty ratio by minimizing a single-objective cost function based on the ESD current and used a comparative logic to regulate the NP voltage. However, the implementation did not realize the dc bus voltage regulation and required iterations to obtain the optimum duty ratio.

Therefore, the main aim of this article is to propose a single-objective modulated model predictive control (SO-M^{2}PC) for a bidirectional dc-dc FC converter that ensures a fixed switching frequency operation, dynamic dc bus and FC voltage regulations, and bidirectional power flow between the ESD and dc bus. The SO-M^{2}PC initially obtains the duty ratio for each power switch by minimizing a single-objective cost function based on the ESD current. A simple mathematical expression based on the FC voltage error optimizes these obtained duty ratios for the FC voltage regulation. Finally, the PS-PWM modulator translates the optimum duty ratios to appropriate switching signals for each power switch. As a result, the converter realizes its multiple control objectives without weighting factors in the cost function and operate its power switches at a constant switching frequency. The SO-M^{2}PC also utilizes an improved dynamic reference model to generate an appropriate battery current reference for the dc bus voltage regulation and bidirectional power flow. Compared to the dynamic reference model [19], the improved model contains additional parameters to eliminate the steady-state error in the dc bus voltage. A simple procedure for designing these parameters is also overlaid in this article.

The rest of this article is organized as follows. Section II describes the bidirectional dc–dc FC converter and its operation in a microgrid. Section III presents the proposed SO-M^{2}PC implementation with the improved dynamic reference model. Section IV presents the experimental results of the proposed SO-M^{2}PC on the bidirectional dc–dc FC converter for different case studies. Finally, Section V concludes this article.

II. Bidirectional DC–DC FC Converter

A. Topology and Operation

A three-level bidirectional dc–dc FC converter integrating battery to a dc bus is shown in Fig. 1. The converter consists of four power switches, an input inductor L, FC C_{fc1}, and an output capacitor C_{dc}. The power switch pairs $(S_1, \bar{S_1})$ and $(S_2, \bar{S_2})$ operate in a complementary manner to ensure a short-circuit free path for C_{fc1} and C_{dc}. During converter operation, the FC voltage v_{fc1} is regulated as

$$v_{\mathrm{fc1}} = \frac{v_{\mathrm{dc}}}{2} \tag{1}$$

where v_{dc} is the dc bus voltage. The regulated FC ensures a reduced voltage stress of $\frac{v_{\mathrm{dc}}}{2}$ across its power switches, unlike

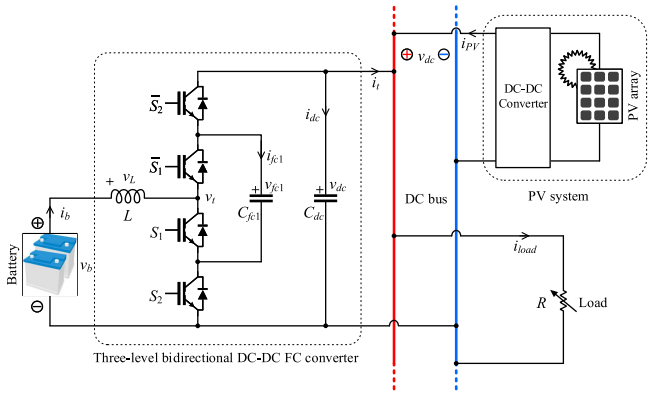

Fig. 1. Three-level bidirectional dc–dc FC converter integrating the battery to a dc bus.

TABLE I
THREE-LEVEL BIDIRECTIONAL DC–DC FC CONVERTER: SWITCHING STATES, TERMINAL VOLTAGE, FC CURRENT, AND FC VOLTAGE

State	S_1	S_2	v_t	i_{fc1}	Δv_{fc1}	
					$i_b > 0$	$i_b < 0$
I	0	0	v_{dc}	0	-	-
II	0	1	v_{fc1}	i_b	↑	↓
III	1	0	$v_{dc} - v_{fc1}$	$-i_b$	↓	↑
IV	1	1	0	0	-	-

the conventional bidirectional dc–dc converter, where its power switches encounter maximum voltage stress of $v_{\rm dc}$.

All possible switching states with the converter terminal voltage v_t and FC current $i_{\rm fc1}$ are shown in Table I. It is seen that the converter has four possible states with three distinct voltage levels 0, $\frac{v_{\rm dc}}{2}$, and $v_{\rm dc}$. The level $\frac{v_{\rm dc}}{2}$ has two redundant states II and III, which affects $v_{\rm fc1}$ depending on the direction of the battery current i_b (see Table I). The converter operation mode is determined by the direction of i_b. The converter operates in boost mode when $i_b > 0$, and in buck mode when $i_b < 0$. The boost mode facilitates a power flow from the battery to the dc bus, while the buck mode facilitates a power flow from the dc bus to the battery. The converter operation with its steady-state waveforms during boost and buck modes are shown in Fig. 2. The duty ratio d of the power switches can be expressed as

$$d = 1 - 2\left(\frac{v_{\rm dc}}{v_b}\right)^{-1} \tag{2}$$

where v_b is the battery voltage. The S_1 and S_2 are generated by comparing d with triangular carriers C_1 and C_2 of frequency f_s, respectively, as shown in Fig. 2. It is seen that the state selection is determined by d, which is a function of the converter voltage-gain ratio $\frac{v_{\rm dc}}{v_b}$ (2). To attain a voltage-gain conversion above 2, the converter operates in the range $0 \le d \le 1$ (region R_1) and generates level 0 and $\frac{v_{\rm dc}}{2}$ by utilizing states IV and II/III, respectively. Similarly, for a voltage-gain between 1 and 2, the converter operates in the range $-1 \le d \le 0$ (region R_2) and generates level $\frac{v_{\rm dc}}{2}$ and $v_{\rm dc}$ by utilizing II/III and I, respectively.

Unlike the conventional bidirectional dc-dc converter, the frequency of the battery current ripple Δi_b for a three-level bidirectional dc-dc FC converter is observed to be twice the

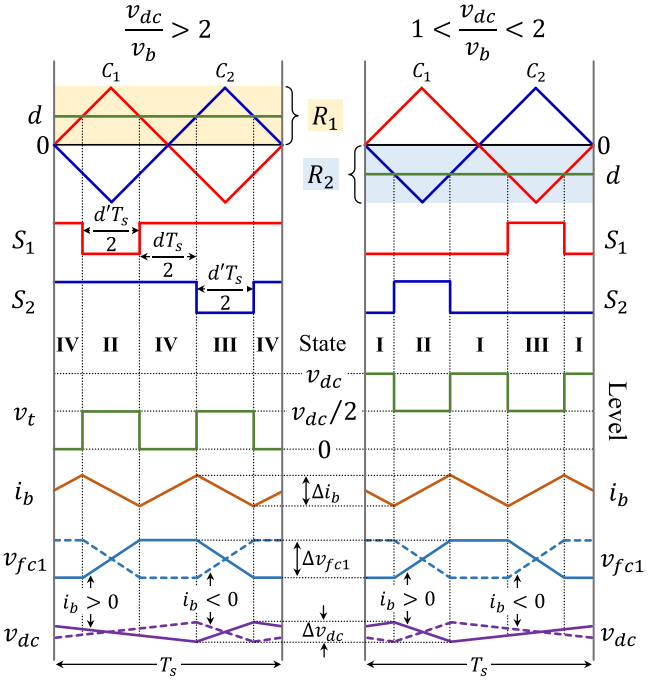

Fig. 2. Steady-state waveforms of a three-level bidirectional dc-dc FC converter operating at $\frac{v_{\rm dc}}{v_b} > 2$ and $1 < \frac{v_{\rm dc}}{v_b} < 2$.

switching frequency f_s (see Fig. 2). As a result, the converter requires a low-sized inductor filter at its input. From Fig. 2, Δi_b can be expressed as

$$\Delta i_b = \frac{v_b\left(v_{dc} - 2v_b\right)}{2v_{dc}L} T_s. \tag{3}$$

Thus, the value of L is designed based on the desired Δi_b. Similarly, the values of $C_{\rm fc1}$ and $C_{\rm dc}$ are designed using the FC voltage ripple $\Delta v_{\rm fc1}$ and dc bus voltage ripple $\Delta v_{\rm dc}$, respectively, which can be obtained from Fig. 2 as

$$\Delta v_{\rm fc1} = \frac{v_b i_b}{v_{\rm dc} C_{\rm fc1}} T_s \tag{4}$$

and

$$\Delta v_{\rm dc} = \frac{v_b i_b\left(v_{\rm dc} - v_b\right)}{v_{\rm dc}^2 C_{\rm dc}} T_s. \tag{5}$$

It is seen that $\Delta v_{\rm fc1}$ and $\Delta v_{\rm dc}$ is directly proportional to the magnitude of i_b. Thus, the values of $C_{\rm fc1}$ and $C_{\rm dc}$ are designed for the maximum rated i_b.

B. Control Objectives

Besides the battery system, the dc bus is also connected to a load and a PV system that harvests maximum power depending on the available solar irradiance (see Fig. 1). Due to uncertainties in the PV power injection and load variation, the dc bus voltage varies abnormally and subject to failure/misoperation of other connected loads in the dc bus if not regulated. Also, the converter requires its power switches to operate at a constant switching frequency and regulate its FC voltage (1) for ensuring operational safety. Therefore, the control objectives are to operate at a fixed switching frequency, regulate the dc bus and FC voltage, and

control a bidirectional power flow between the battery and dc bus.

III. Proposed SO-M^{2}PC Implementation

A. Converter Mathematical Model

The v_t in terms of $v_{\rm dc}$ and $v_{\rm fc1}$ can be expressed as

$$v_t = (d_2 - d_1)v_{\rm fc1} + (1 - d_2)v_{\rm dc} \tag{6}$$

where d_1 and d_2 are the duty ratio of power switches S_1 and S_2, respectively. The continuous-time model of the converter in terms of its variable $\mathbf{x} = [i_b\ v_{\rm fc1}\ v_{\rm dc}]^T$ is expressed as

$$\dot{\mathbf{x}} = \begin{bmatrix} 0 & \frac{d_1-d_2}{L} & \frac{d_2-1}{L} \\ \frac{d_2-d_1}{C_{\rm fc1}} & 0 & 0 \\ \frac{1-d_2}{C_{\rm dc}} & 0 & \frac{-1}{RC_{\rm dc}} \end{bmatrix} \mathbf{x} + \begin{bmatrix} \frac{1}{L} & 0 \\ 0 & 0 \\ 0 & \frac{1}{C_{\rm dc}} \end{bmatrix} \begin{bmatrix} v_b \\ i_{\rm PV} \end{bmatrix} \tag{7}$$

where R is the load resistance and $i_{\rm PV}$ is the PV system current. Equation (7) is discretized using the forward Euler method. Thus, the predicted battery current i_b^{k+1} can be written as

$$i_b^{k+1} = i_b^k + \frac{T_s}{L}\left(v_b^k - (d_2^k - d_1^k)v_{\rm fc1}^k - (1 - d_2^k)v_{\rm dc}^k\right) \tag{8}$$

where T_s is the controller sampling period. The terms v_b^k and v_{dc}^k are the battery and dc bus voltage measured at the time instant k. Therefore, (8) is used in the proposed controller to obtain d_1^k and d_2^k for a time period T_s such that i_b^{k+1} attains the battery current reference.

B. Cost Function Formulation

The proposed controller optimizes a single-objective cost function based on the battery current. This is accomplished by minimizing the battery current error every T_s. As a result, a quadratic single-objective cost function is formulated as

$$J^k = (i_b^{*k+1} - i_b^{k+1})^2 \tag{9}$$

where i_b^{*k+1} is the battery current reference to be attained by the converter for the time instant $k+1$. An improved dynamic reference model is used to generate the i_b^{*k+1}.

C. Dynamic Reference Model

The dynamic reference model generates appropriate i_b^* for the dc bus voltage regulation and bidirectional power flow. The i_b^* is determined from the power supplied/absorbed by the battery for regulating the $v_{\rm dc}$ to $V_{\rm dc}^*$. Instead of using a constant reference $V_{\rm dc}^*$, a time-varying dc bus voltage reference $v_{\rm dc}^*$ was introduced in [19] to generate i_b^*. This ensured a dynamic control of $v_{\rm dc}$ to $V_{\rm dc}^*$ without introducing undesirable fluctuations in i_b^*. However, such an implementation always had a steady-state error in the $v_{\rm dc}$. Thus, the dynamic reference model [19] is improved by introducing an additional term that adds the dc bus voltage error over time and eliminates the prevailing steady state in $v_{\rm dc}$. The improved discrete-time model for $v_{\rm dc}^*$ in terms of $V_{\rm dc}^*$ is given as

$$v_{\rm dc}^{*k+1} = v_{\rm dc}^k + \frac{V_{\rm dc}^* - v_{\rm dc}^k}{N_R} + \frac{A^k}{N_L} \tag{10}$$

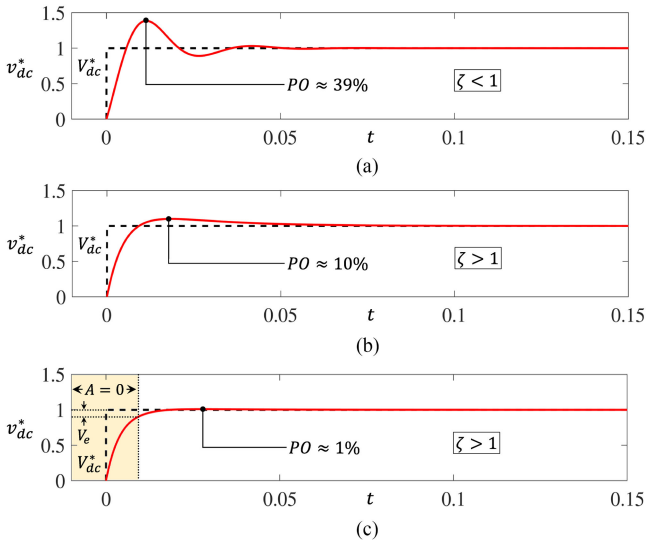

Fig. 3. Step response of improved dynamic reference model for: (a) $N_R = 600$, $N_L = 2 \times 10^5$, $V_e = V_{\rm dc}^*$, (b) $N_R = 400$, $N_L = 10^6$, $V_e = V_{\rm dc}^*$, and (c) $N_R = 400$, $N_L = 10^6$, $V_e = 0.1V_{\rm dc}^*$.

and

$$A^k = \begin{cases} 0, & \text{if } V_e < |V_{\rm dc}^* - v_{\rm dc}^k| \\ A^{k-1} + V_{\rm dc}^* - v_{\rm dc}^k, & \text{if } V_e \geq |V_{\rm dc}^* - v_{\rm dc}^k| \end{cases} \tag{11}$$

where N_R and N_L are the parameters that decide the dynamics for $v_{\rm dc}^*$ and V_e is a parameter that decides the value of A^k based on the dc bus voltage error $|V_{\rm dc}^* - v_{\rm dc}^k|$.

To analyze the effect of N_R, N_L, and V_e on the dynamics of $v_{\rm dc}^*$, a continuous-time model of (10) is derived by considering $v_{\rm dc}^k = v_{\rm dc}^{*k}$ and $V_e = V_{\rm dc}^*$. Thus, (10) can be rewritten as

$$\Delta v_{\rm dc}^*(t) = \frac{V_{\rm dc}^* - v_{\rm dc}^*(t)}{N_R} + \frac{1}{T_s}\int_0^\infty \frac{V_{\rm dc}^* - v_{\rm dc}^*(t)}{N_L} dt. \tag{12}$$

Furthermore, dividing (12) by T_s and differentiating with respect to time gives the characteristic equation of (10) as

$$\frac{d^2 v_{\rm dc}^*(t)}{dt^2} + \frac{1}{N_R T_s}\frac{dv_{\rm dc}^*(t)}{dt} + \frac{1}{N_L T_s^2} v_{\rm dc}^*(t) = 0. \tag{13}$$

It is seen that the improved dynamic reference model is a second-order system. On comparing the coefficients of (13) with the standard definition[1] of a second-order system, the damping-factor ζ can be expressed as

$$\zeta = \frac{\sqrt{N_L}}{2N_R}. \tag{14}$$

The value of ζ quantifies the nature of $v_{\rm dc}^*$ response. The model with $\zeta < 1$ generates an oscillatory $v_{\rm dc}^*$ with significant overshoot as shown in Fig. 3(a). Such an oscillatory $v_{\rm dc}^*$ is not desirable and is damped by selecting N_R and N_L values such that $\zeta > 1$ [see Fig. 3(b)]. Even though a nonoscillatory $v_{\rm dc}^*$ is

[1]The differential equation of a second-order system $x(t)$ is defined as: $\frac{d^2x(t)}{dt^2} + 2\zeta\omega_n\frac{dx(t)}{dt} + \omega_n^2 x(t) = 0$, where ζ is the damping ratio and ω_n is the natural frequency of the system [32]. From (13), the coefficients of the differential equation can be written as: $2\zeta\omega_n = \frac{1}{N_R T_s}$ and $\omega_n^2 = \frac{1}{N_L T_s^2}$. On simplifying, ζ can be obtained as shown in (14).

generated, the percentage overshoot PO of 10% is observed in its response. Through proper selection of V_e, the PO in v_{dc}^* can be reduced. The step response of the same model ($N_R = 400$ and $N_L = 10^6$) with $V_e = 0.1V_{\text{dc}}^*$ is shown in Fig. 3(c). When the dc bus voltage error is greater than V_e, $A = 0$. As a result, the model generates v_{dc}^* using N_R alone [shaded region in Fig. 3(c)]. When the dc bus voltage error falls less than V_e, A adds up the dc bus voltage error and incorporates N_L for generating v_{dc}^*. Compared to the model in Fig. 3(b), the PO in Fig. 3(c) is observed to reduce by a factor of $\frac{V_e}{V_{\text{dc}}^*}$. In summary, the N_R and N_L values are selected such that $\zeta > 1$ and V_e is chosen based on the desired PO in v_{dc}^*. In doing so, a smooth convergence of v_{dc} to V_{dc}^* is ensured without introducing undesirable oscillations and overshoots, as shown in Fig. 3(c).

The discrete-time equation for the reference dc bus capacitor current i_{dc}^* and reference load current i_{load}^* in terms of v_{dc}^* can be written as

$$i_{\text{dc}}^{*k+1} = \frac{C_{\text{dc}}}{T_s}\left(v_{\text{dc}}^{*k+1} - v_{\text{dc}}^{k}\right) \tag{15}$$

and

$$i_{\text{load}}^{*k+1} = \frac{v_{\text{dc}}^{*k+1}}{R^k}, \text{ where } R^k = \frac{v_{\text{dc}}^{k}}{i_{load}^{k}} \tag{16}$$

where i_{load}^k is the dc bus load current measured at time instant k, and R^k is the estimated load resistance at time instant k. On applying power balance between the battery and dc bus (assuming zero converter losses), the discrete-time equation for i_b^* can be expressed as

$$i_b^{*k+1} = \frac{v_{\text{dc}}^{*k+1}}{v_b^k}\left(i_{\text{dc}}^{*k+1} + i_{\text{load}}^{*k+1} - i_{\text{PV}}^{k}\right) \tag{17}$$

where i_{PV}^k is the PV current measured at time instant k. It is observed that i_b^{*k+1} changes with respect to v_b^k, i_{load}^k, and i_{PV}^k. The converter operates in boost mode when $i_b^{*k+1} > 0$ ($i_{\text{load}}^{*k+1} > i_{\text{PV}}^k$), and buck mode when $i_b^{*k+1} < 0$ ($i_{\text{load}}^{*k+1} < i_{\text{PV}}^k$). Thus, allowing the converter to perform a bidirectional power flow between the battery and dc bus effectively, during uncertainties in PV power injection and/or load variations.

D. Proposed SO-M^{2}PC Algorithm

The block diagram of the proposed SO-M^{2}PC for a three-level bidirectional dc–dc FC converter is shown in Fig. 4. The proposed controller operates at the rate of T_s. The controller initially determines duty ratio d_1^k and d_2^k to attain i_b^{*k+1}. Further, the obtained duty ratios are adjusted by a factor Δd^k to attain FC voltage regulation to V_{fc1}^*. Finally, the optimum duty ratios $d_{1\text{opt}}^k = d_1^k + \Delta d^k$ and $d_{2\text{opt}}^k = d_2^k - \Delta d^k$ are sent to the PS-PWM modulator that generates appropriate switching signals for the power switches. The procedure for obtaining d_1^k, d_2^k, and Δd^k are explained in separate sections.

1) Duty Ratio Computation: The d_1^k and d_2^k are obtained by minimizing J^k (9). Thus, the mathematical definition of minimization performed on J^k at time instant k is expressed as

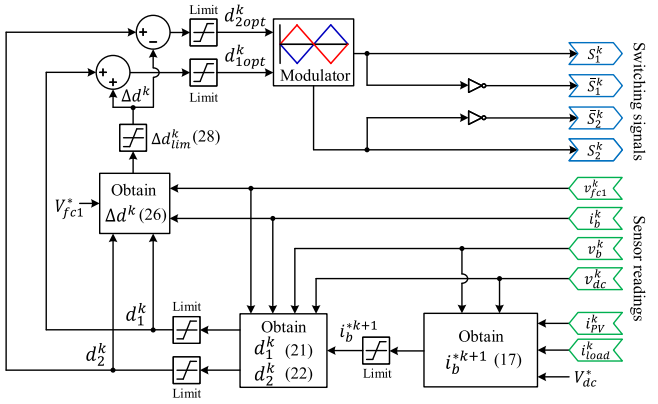

Fig. 4. Block diagram of SO-M^{2}PC implementation for a three-level bidirectional dc–dc FC converter in a microgrid.

$$\arg\min_{d_1^k, d_2^k} J^k(d_1^k, d_2^k). \tag{18}$$

Since J^k is a function of d_1^k and d_2^k, (18) is minimized by equating the partial derivative of J^k with respect to d_1^k and d_2^k to zero. Observe that during one half of T_s in Fig. 2, S_1 is modulating with S_2 as constant, while in another half of T_s, S_2 is modulating with S_1 as constant. Therefore, the partial derivative of J^k with respect to d_1^k and d_2^k can be expressed as

$$\left.\frac{\partial J^k}{\partial d_1^k}\right|_{d_2^k=1} = 2\left(i_b^{*k+1} - i_b^{k+1}\right)\left(\frac{\partial i_b^{*k+1}}{\partial d_1^k} - \frac{\partial i_b^{k+1}}{\partial d_1^k}\right) \tag{19}$$

and

$$\left.\frac{\partial J^k}{\partial d_2^k}\right|_{d_1^k=1} = 2\left(i_b^{*k+1} - i_b^{k+1}\right)\left(\frac{\partial i_b^{*k+1}}{\partial d_2^k} - \frac{\partial i_b^{k+1}}{\partial d_2^k}\right). \tag{20}$$

On equating (19) and (20) to zero, d_1^k and d_2^k can be obtained as

$$d_1^k = 1 - \frac{v_b^k}{v_{\text{fc1}}^k} + \frac{L}{T_s}\left(\frac{i_b^{*k+1} - i_b^k}{v_{\text{fc1}}^k}\right) \tag{21}$$

and

$$d_2^k = 1 - \frac{v_b^k}{v_{\text{dc}}^k - v_{\text{fc1}}^k} + \frac{L}{T_s}\left(\frac{i_b^{*k+1} - i_b^k}{v_{\text{dc}}^k - v_{\text{fc1}}^k}\right). \tag{22}$$

During a steady-state operation, $(i_b^{*k+1} - i_b^k) \approx 0$, $v_{\text{fc1}}^k \approx \frac{V_{\text{dc}}^*}{2}$, and $v_{\text{dc}}^k \approx V_{\text{dc}}^*$, leading to $d_1^k \approx d_2^k$. This scenario is demonstrated between time interval t_0 and t_1 in Fig. 5. It can be seen that d_1^k and d_2^k obtained from (21) and (22) are solely based on battery current minimization and does not guarantee FC voltage regulation (see Fig. 5). Therefore, calculated d_1^k and d_2^k require further adjustments to realize the FC voltage regulation.

2) FC Voltage Regulation: The obtained d_1^k and d_2^k is adjusted by Δd^k such that the average FC voltage $v_{\text{fc1}a}$ becomes V_{fc1}^* in a T_s. The effect of Δd^k on v_{fc1} during boost operation mode is shown in Fig. 5. Thus, the $v_{\text{fc1}a}$ for a given T_s can be

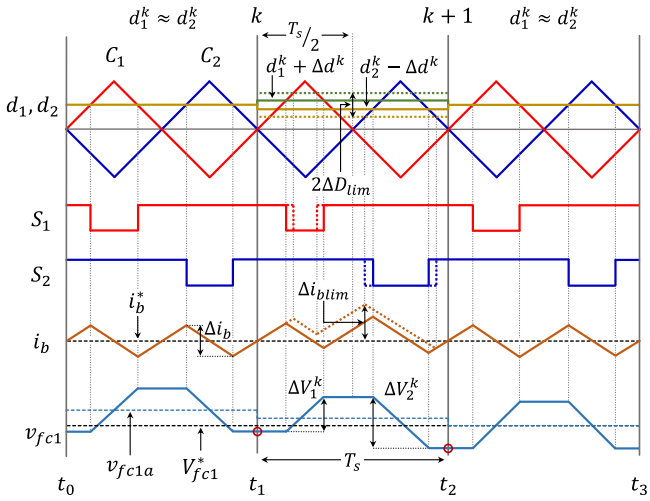

Fig. 5. Effect of duty ratios on FC voltage regulation during the boost mode.

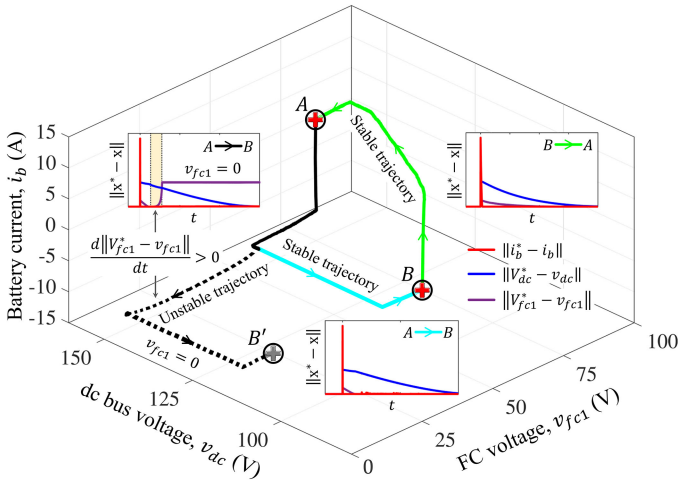

Fig. 6. Stability evaluation of the proposed SO-M^{2}PC based on system variable convergence during a step change in the operating point.

expressed in terms of v_{fc1}^k as

$$v_{\text{fc1}a} = v_{\text{fc1}}^k + 3\frac{\Delta V_1^k}{4} - \frac{\Delta V_2^k}{4} \tag{23}$$

where ΔV_1^k and ΔV_2^k can be expressed in terms of their respective duty ratio as

$$\Delta V_1^k = \frac{(1 - d_1^k - \Delta d^k)T_s}{2C_{\text{fc1}}} i_b^k \tag{24}$$

and

$$\Delta V_2^k = \frac{(1 - d_2^k + \Delta d^k)T_s}{2C_{\text{fc1}}} i_b^k. \tag{25}$$

Since the objective is to attain $v_{\text{fc1}a} = V_{\text{fc1}}^*$, the required Δd^k can be obtained by rewriting (23) as

$$\Delta d^k = \frac{1}{2} - 3\frac{|d_1^k|}{4} + \frac{|d_2^k|}{4} - \frac{2C_{\text{fc1}}}{T_s i_b^k}(V_{\text{fc1}}^* - v_{\text{fc1}}^k). \tag{26}$$

The resulting value of Δd^k determines the level of adjustment required in d_1^k and d_2^k for regulating the v_{fc1} in a T_s. However, such duty ratio adjustments can cause deviation in i_b from i_b^* as shown in Fig. 5. Note that the i_b deviation becomes severe if the obtained Δd^k from (26) is large. Thus, the Δd^k is required to be limited to ΔD_{lim} such that the peak deviation in i_b from i_b^* is always within the desirable limit $\Delta i_{b\text{lim}}$ (see Fig. 5). The ΔD_{lim} in terms of the $\Delta i_{b\text{lim}}$ is derived from Fig. 5 and expressed as

$$\Delta D_{\text{lim}} = \pm\frac{2L}{T_s}\left(\frac{2\Delta i_{b\text{lim}} - \Delta i_b}{V_{\text{dc}}^* - v_b}\right). \tag{27}$$

In this article, $\Delta i_{b\text{lim}} = 0.21$A is considered, which on substituting into (27) gives $\Delta D_{\text{lim}} = \pm 0.06$. In doing so, v_{fc1} is regulated to V_{fc1}^* without introducing undesirable deviations in i_b. Note that ΔD_{lim} also affects the dynamics of v_{fc1} and its convergence to V_{fc1}^* during a step response. The v_{fc1} demonstrates a faster convergence to V_{fc1}^* for large ΔD_{lim}. However, usage of large ΔD_{lim} generates significant ripple in i_b during the steady state, which can deteriorate the battery health. Hence, ΔD_{lim} is decided using (27) based on the desired $\Delta i_{b\text{lim}}$.

E. Stability Evaluation

To evaluate the stability of SO-M^{2}PC, the effect of the converter variables during a step change in its operating point is studied. Fig. 6 shows the trajectory of its variables in a 3-D space with its Euclidean norm, $||\mathbf{x}^* - \mathbf{x}||$ during a step change in the operating point. The $||\mathbf{x}^* - \mathbf{x}||$ defines the distance between variable $\mathbf{x}$ from its reference $\mathbf{x}^*$. For a stable convergence of $\mathbf{x}$ to $\mathbf{x}^*$, the $\lim_{t\to\infty} ||\mathbf{x}^* - \mathbf{x}|| = 0$ must be satisfied. Consider the converter operating at point B ($v_{\text{dc}} = 100$ V, $v_{\text{fc1}} = 50$ V, and $i_b = -4.5$ A), undergoes a step-change to point A ($v_{\text{dc}} = 150$ V, $v_{\text{fc1}} = 75$ V, and $i_b = 4.5$ A). A stable trajectory is observed in Fig. 6 with $\frac{d||\mathbf{x}^* - \mathbf{x}||}{dt} < 0$ during the transition from B to A. Thus, ensuring a stable convergence of the variables to its reference. However, when the converter undergoes a step change from A to B, the trajectory is observed to deflect away from the reference point B and settle down to another point B' ($v_{\text{dc}} = 101.5$ V, $v_{\text{fc1}} = 0$ V, and $i_b = -4.5$ A). This is because the ΔD_{lim} restricts the Δd^k (26) from providing necessary adjustments to d_1^k and d_2^k for the FC voltage regulation when $\frac{d||V_{\text{fc1}}^* - v_{\text{fc1}}||}{dt} > 0$. As a result, v_{fc1} fails to converge to V_{fc1}^* and becomes zero (see Fig. 6). To ensure a stable convergence of v_{fc1} to V_{fc1}^*, the limit for Δd^k has to be relaxed based on the change in $||V_{\text{fc1}}^* - v_{\text{fc1}}^k||$. Thus, Δd_{lim}^k is introduced, which is defined as

$$\Delta d_{\text{lim}}^k = \begin{cases} \pm\infty, \text{ if } e^k < e^{k-1},\ e^k < 0, \text{ and } e^{k-1} < 0, \text{ where} \\ \Delta D_{\text{lim}}, \text{ otherwise.} \end{cases} \tag{28}$$

$$e^k = ||V_{\text{fc1}}^* - v_{\text{fc1}}^{k-1}|| - ||V_{\text{fc1}}^* - v_{\text{fc1}}^k||. \tag{29}$$

It can be seen that the Δd^k is not limited to ΔD_{lim} when $\frac{d||V_{\text{fc1}}^* - v_{\text{fc1}}||}{dt} > 0$. In doing so, a stable trajectory with $\frac{d||\mathbf{x}^* - \mathbf{x}||}{dt} < 0$ is ensured during the transition from A to B, as shown in Fig. 6. Hence, the proposed SO-M^{2}PC implementation summarized in Fig. 4 guarantees a stable convergence of the variables to its reference.

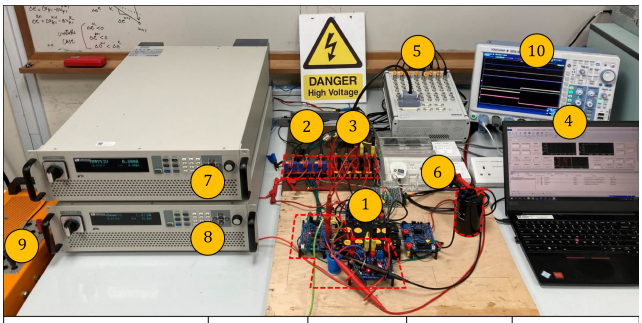

1. Three-level bidirectional DC-DC FC converter	2. Current sensors	3. Voltage sensors	4. Host PC	5. dSPACE MicroLabBox
6. DC bus capacitor C_{dc}	7. PV emulator	8. Battery emulator	9. Load	10. Oscilloscope

Fig. 7. Photograph of the experimental setup.

TABLE II
PARAMETERS FOR EXPERIMENTAL TEST

System and control parameters				
V_{dc}^*	V_{fc1}^*	v_b	V_e	T_s
100V	50V	25V	3.3V	100μs
C_{dc}	C_{fc1}	L	N_R	N_L
2.2mF	470μF	2mH	200	10^6
Load condition for different time instances				
Case	$t(s)$	$R(\Omega)$		
1 *4*	$0-2$ $0-10$	200		
2	$0-6$ and $14-20$ $6-14$	50 100		
3	$0-50$	100		

IV. EXPERIMENTAL RESULTS

The proposed SO-M^{2}PC is validated experimentally on a low-power three-level bidirectional dc-dc FC converter that was developed using four SiC MOSFET C2M0025120D as shown in Fig. 7. One of the two sets of ITECH IT-6006 C programmable dc power sources is used to emulate as a battery and another as a PV system. The IT-6006 C used to emulate the PV system is configured such that the PV array achieves its maximum power P_m during the operation. Since $v_{\rm dc}$ is regulated by the bidirectional dc–dc FC converter, the IT-6006 C is configured to operate at a constant current mode with its current set to $P_m/v_{\rm dc}$. As a result, the IT-6006 C delivers maximum power to the dc bus just as it would when the PV system operates with the traditional MPPT algorithm. The proposed controller is programmed using a function block in MATLAB/Simulink and is implemented experimentally using the dSPACE MicroLabBox controller. The system parameters considered for the experiment are given in Table II. The value of L is designed to limit Δi_b (3) to 5% of $I_{b\rm max} = 6$A, while the value of $C_{\rm fc1}$ and $C_{\rm dc}$ are designed for $i_b = I_{b\rm max}$ such that $\Delta v_{\rm fc1}$ (4) and $\Delta v_{\rm dc}$ (5) are limited to 0.75% and 0.05%, respectively. Analysis of the dc bus and FC voltage regulation during a step response of the dc bus voltage, load, PV power, system parameter variations are studied to assess the effectiveness of the proposed SO-M^{2}PC. Furthermore, analysis on the converter's performance during a step response with the FCS-MPC approach is demonstrated and compared with the proposed SO-M^{2}PC.

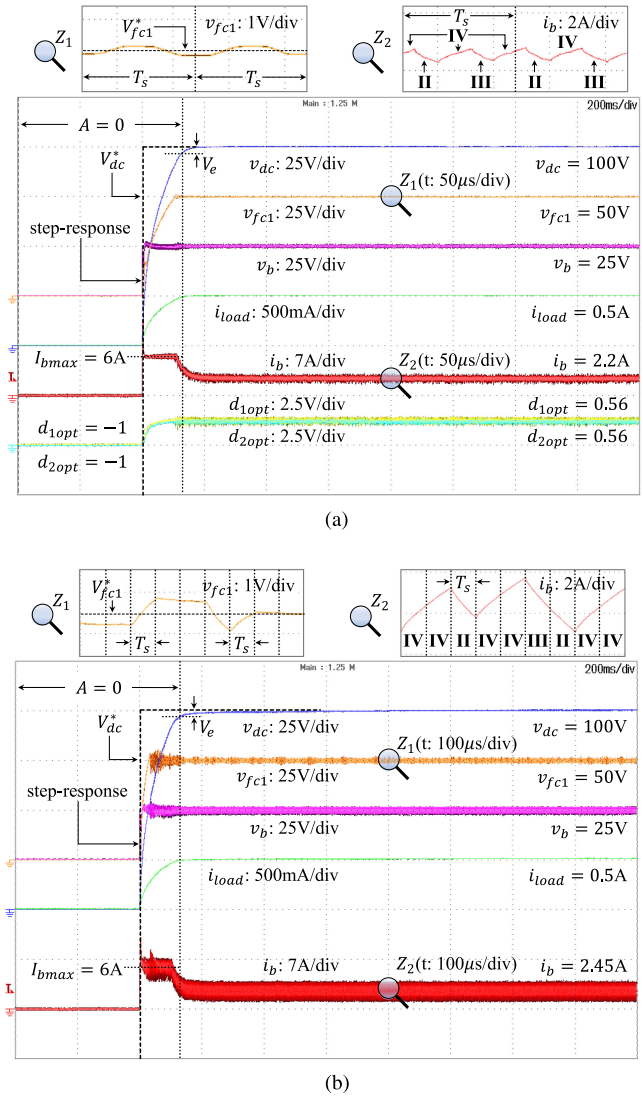

Fig. 8. Performance of a three-level bidirectional dc-dc FC converter during a step response of $v_{\rm dc}$ using (a) proposed SO-M^{2}PC and (b) FCS-MPC.

A. Case 1: Comparative Analysis of SO-M^{2}PC With FCS-MPC

The converter's performance with the proposed SO-M^{2}PC and FCS-MPC [17] for a step response of the dc bus voltage is shown in Fig. 8(a) and (b), respectively. Until $t = 400$ ms, all variables of the system are zero. Note that the PV system is not considered in this article and does not contribute power to the dc bus ($i_{\rm PV} = 0$). At $t = 400$ ms, v_b is switched-ON and the controller is activated. It can be observed from Fig. 8(a) that the $d_{1\rm opt}$ and $d_{2\rm opt}$ obtained by the SO-M^{2}PC have a smooth trajectory before settling to a steady-state value. As a result, $v_{\rm dc}$ and $v_{\rm fc1}$ are observed to rise steadily and converge to $V_{\rm dc}^*$ and $V_{\rm fc1}^*$, respectively, without any undesirable disturbances. The zoomed view of i_b and $v_{\rm fc1}$ for two sampling periods are also shown in Fig. 8(a). The $d_{1\rm opt}$ and $d_{2\rm opt}$ are translated to

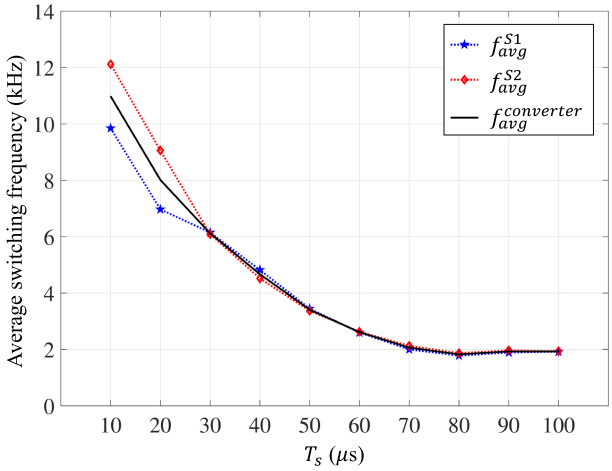

Fig. 9. Average switching frequency of the converter and its power switches operating with FCS-MPC at different T_s.

switching signals by a PS-PWM modulator, as illustrated in Fig. 4. This enables the SO-M^{2}PC to apply a fixed sequence of states II–IV in a T_s. Thus, all the power switches in the converter operate at a fixed frequency of 10 kHz and impart equal switching loss. Also, the Δi_b and $\Delta v_{\rm fc1}$ are observed to be within the desirable limits of 5% and 0.75%, respectively.

On the other hand, the FCS-MPC is observed to apply only one optimum state per T_s to realize the control objectives [see Fig. 8(b)]. As a result, an operation with a fixed sequence of states is not guaranteed, as seen for the SO-M^{2}PC [see Fig. 8(a)]. Unlike the SO-M^{2}PC, the FCS-MPC with $T_s = 100\,\mu$s operates the converter at an average switching frequency of 2 kHz. As a result, the system variables are observed to have a large ripple. Compared to the SO-M^{2}PC, the Δi_b and $\Delta v_{\rm fc1}$ are increased by 95% and 234%, respectively. The presence of such a huge ripple can overheat the battery and deteriorate its life cycle. Thus, the FCS-MPC is required to either operate at a smaller T_s or with large parameter values to reduce the ripple in the variables. The effect of the converter's average switching frequency with FCS-MPC under different T_s is shown in Fig. 9. It is seen that the FCS-MPC should operate at $T_s = 13\,\mu$s to match its average switching frequency with the SO-M^{2}PC. Thus, requiring a high-speed controller for its implementation. Also, the average switching frequency of S_2 is observed to be greater than the average switching frequency of S_1 for FCS-MPC with a smaller T_s (see Fig. 9). Such difference in the average switching frequency of individual power switches not only subjects an improper switching loss distribution but also causes an unequal erosion of the power switches in the converter. Thus, reducing the reliability of the system.

The variable switching frequency in FCS-MPC can be dealt with by incorporating a switching minimization term in its cost function through the weighting factor. However, this requires an appropriate estimation and does not guarantee a fixed switching frequency in all operating scenarios. In addition, the FCS-MPC takes 1.4 μs to identify the optimum state by searching through a finite set of four possible states (see Table I), while the proposed SO-M^{2}PC identifies the optimum duty ratios in only 0.84 μs as it utilizes simplified mathematical expressions. As the converter level n increases, the computational burden of FCS-MPC rises

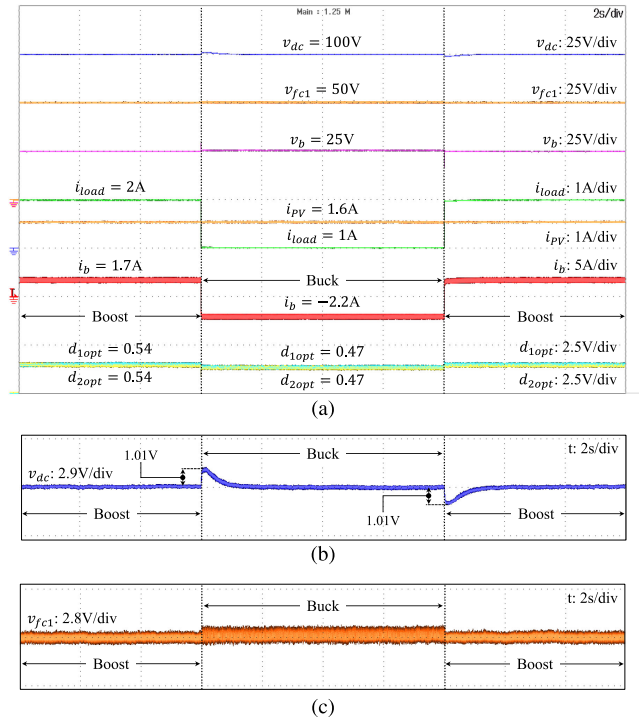

Fig. 10. (a) Experimental results on the operation of a three-level bi-directional dc–dc FC converter during load variation. (b) Zoomed view of $v_{\rm dc}$. (c) Zoomed view of $v_{\rm fc1}$.

exponentially. This is because of the increase in a finite set of 2^{n-1} possible states. On the other hand, the computational burden of the SO-M^{2}PC has a minimal rise with the increase in n as it executes simple mathematical expressions to obtain the optimum duty ratios. Thus, the proposed SO-M^{2}PC is computationally less intensive than the FCS-MPC. In conclusion, the proposed SO-M^{2}PC outperforms FCS-MPC in terms of implementation, performance, and operation.

B. Case 2: Load Variation

The converter's performance with the SO-M^{2}PC during a step-load change is shown in Fig. 10. In this article, the PV system is considered to supply a constant power to the dc bus. Until $t = 6$ s, the converter operates in boost mode and regulates the dc bus voltage by supplying power from the battery. The zoomed view of $v_{\rm dc}$ and $v_{\rm fc1}$ is shown in Fig. 10(b) and (c), respectively. It is observed that $v_{\rm dc}$ and $v_{\rm fc1}$ are regulated to its reference during the operation. At $t = 6$ s, a step-load change is subjected as shown in Fig. 10(a). Since the PV system injects power exceeding the load demand ($i_{\rm PV} > i_{\rm load}$), the SO-M^{2}PC instantly switches the converter to buck mode and regulates the dc bus voltage by transmitting the excess PV power to the battery. The $v_{\rm dc}$ and $v_{\rm fc1}$ are observed to be regulated during the operation. An increase in the FC voltage ripple is observed during a buck mode [see Fig. 10(c)]. This is because of the increase in i_b magnitude during the load variation. Equation (4) demonstrates that $\Delta v_{\rm fc1}$ is directly proportional to the i_b magnitude. As a result, the FC voltage ripple is observed to be affected by the change in i_b magnitude. At $t = 14$ s, a step-load change is subjected [see Fig. 10(a)]. Since the PV system injects power lower than the present load demand ($i_{\rm PV} < i_{\rm load}$), the

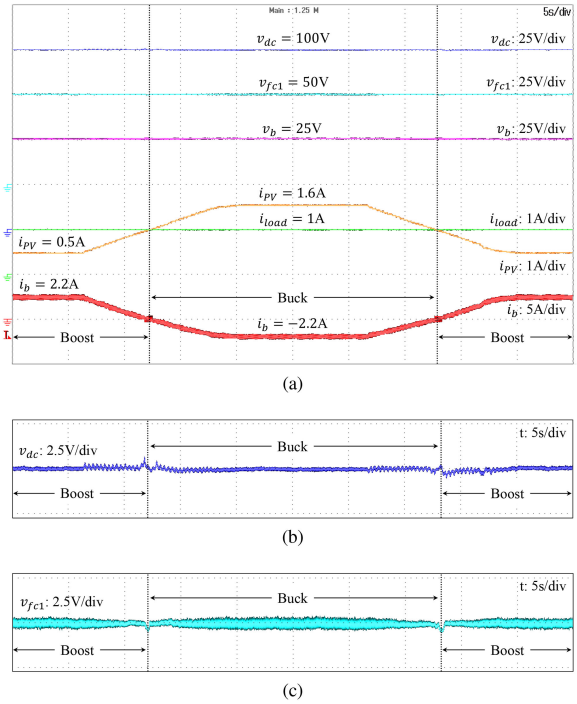

Fig. 11. (a) Experimental results on the operation of a three-level bi-directional dc-dc FC converter during PV power variation. (b) Zoomed view of $v_{\rm dc}$. (c) Zoomed view of $v_{\rm fc1}$.

SO-M^{2}PC instantly switches the converter back to boost mode and regulates the dc bus voltage by supplying the deficit power from the battery. A voltage spike of only 1.01 V is observed in $v_{\rm dc}$ during the mode transitions [see Fig. 10(b)]. The obtained result demonstrates that the proposed SO-M^{2}PC is capable of regulating $v_{\rm dc}$ and $v_{\rm fc1}$ to its reference effectively under load variation.

C. Case 3: PV Power Variation

The converter's performance with the SO-M^{2}PC during PV power variation is shown in Fig. 11. In this article, the load connected across the dc bus is kept constant. Until $t = 12$ s, the PV system supplies power less than the load demand ($i_{\rm PV} < i_{\rm load}$). The SO-M^{2}PC operates the converter in boost mode and regulates the dc bus voltage by supplying deficit power from the battery. The zoomed view of $v_{\rm dc}$ and $v_{\rm fc1}$ is shown in Fig. 11(b) and (c), respectively. It is observed that $v_{\rm dc}$ and $v_{\rm fc1}$ are regulated to its reference during the operation. At $t = 12$ s, the PV power injection exceeds the load demand ($i_{\rm PV} > i_{\rm load}$). The SO-M^{2}PC switches the converter to buck mode and regulates the dc bus voltage by transmitting excess power to the battery. At $t = 38$ s, the PV system supplies power less than the load demand and the converter is toggled back to boost mode. The $v_{\rm dc}$ and $v_{\rm fc1}$ are observed to be regulated throughout its operation. The FC voltage ripple is observed to vary throughout the operation [see Fig. 11(c)]. This is due to the varying i_b magnitude caused by the PV power variation. As illustrated in (4), the $\Delta v_{\rm fc1}$ is directly proportional to i_b magnitude. Therefore, the FC voltage ripple is observed to be large at the instances when i_b magnitude is maximum. The obtained result demonstrates that the proposed

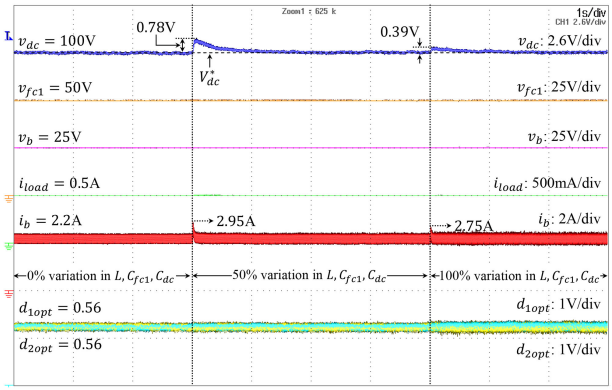

Fig. 12. Experimental results on the performance of the SO-M^{2}PC during parameter variation.

SO-M^{2}PC is capable of regulating $v_{\rm dc}$ and $v_{\rm fc1}$ to its reference effectively under PV power variation.

D. Case 4: Parameter Variation

The converter's performance with the SO-M^{2}PC during the variation in system parameters L, $C_{\rm fc1}$, and $C_{\rm dc}$ is shown in Fig. 12. The experiment is performed by introducing 50% and 100% variation between the system and model parameters. Until $t = 3$ s, the converter operates in a steady state with zero variation in its parameters. At $t = 3$ s, the L, $C_{\rm fc1}$, and $C_{\rm dc}$ are increased by 50%. The change in parameter introduces deviation in the $v_{\rm dc}$ and i_b as shown in Fig. 12. The SO-M^{2}PC identifies these deviations and provide necessary correction to $d_{1\rm opt}$ and $d_{2\rm opt}$ for counteracting the parameter variation. As a result, the ripple in $d_{1\rm opt}$ and $d_{2\rm opt}$ increases, and the system variables converge back to its reference. A similar observation is made at $t = 7$ s, where the L, $C_{\rm fc1}$, and $C_{\rm dc}$ are increased by 100%. The ripple in $d_{1\rm opt}$ and $d_{2\rm opt}$ is observed to increase with the rise in parameter variation (see Fig. 12). Thus, the SO-M^{2}PC is capable of realizing its multiple control objectives during a parameter variation.

V. Conclusion

An SO-M^{2}PC for a bidirectional dc–dc FC converter integrating the battery to a microgrid was proposed in this article. Unlike FCS-MPC, the proposed SO-M^{2}PC determined the optimum duty ratio for the power switches by using a single-objective cost function to attain multiple control objectives, i.e., dc bus and FC voltage regulation and bidirectional power flow. The SO-M^{2}PC first obtained the duty ratio for the power switches by minimizing the battery current, and then, necessary corrections were provided on the obtained duty ratio based on the FC voltage error. It was validated from the experimental result that the proposed SO-M^{2}PC outperformed the FCS-MPC by operating the power switches at a fixed frequency and fulfilled multiple control objectives without any weighting factor in the cost function. The SO-M^{2}PC was also free from the secondary control loop as it utilized an improved dynamic reference model to generate the appropriate battery current reference for the dc bus voltage regulation and bidirectional power flow. Furthermore, experimental validation of the proposed SO-M^{2}PC for load, PV

power, and system parameter variation were demonstrated to prove the effectiveness of the proposed controller in a microgrid.

REFERENCES

[1] J. Pegueroles-Queralt, F. D. Bianchi, and O. Gomis-Bellmunt, "A power smoothing system based on supercapacitors for renewable distributed generation," *IEEE Trans. Ind. Electron.*, vol. 62, no. 1, pp. 343–350, Jan. 2015.

[2] J. Xiao, P. Wang, and L. Setyawan, "Hierarchical control of hybrid energy storage system in DC microgrids," *IEEE Trans. Ind. Electron.*, vol. 62, no. 8, pp. 4915–4924, Aug. 2015.

[3] S. K. Kollimalla, M. K. Mishra, A. Ukil, and H. B. Gooi, "DC grid voltage regulation using new HESS control strategy," *IEEE Trans. Sustain. Energy*, vol. 8, no. 2, pp. 772–781, Apr. 2017.

[4] X. Li, D. Hui, and X. Lai, "Battery energy storage station (BESS)-based smoothing control of photovoltaic (PV) and wind power generation fluctuations," *IEEE Trans. Sustain. Energy*, vol. 4, no. 2, pp. 464–473, Apr. 2013.

[5] N. R. Tummuru, U. Manandhar, A. Ukil, H. B. Gooi, S. K. Kollimalla, and S. Naidu, "Control strategy for AC-DC microgrid with hybrid energy storage under different operating modes," *Int. J. Elect. Power Energy Syst.*, vol. 104, pp. 807–816, Jan. 2019.

[6] K. Sun, L. Zhang, Y. Xing, and J. M. Guerrero, "A distributed control strategy based on DC bus signaling for modular photovoltaic generation systems with battery energy storage," *IEEE Trans. Power Electron.*, vol. 26, no. 10, pp. 3032–3045, Oct. 2011.

[7] G. Wu, X. Ruan, and Z. Ye, "Nonisolated high step-up DC-DC converters adopting switched-capacitor cell," *IEEE Trans. Ind. Electron.*, vol. 62, no. 1, pp. 383–393, Jan. 2015.

[8] H. Kang and H. Cha, "A new nonisolated high-voltage-gain boost converter with inherent output voltage balancing," *IEEE Trans. Ind. Electron.*, vol. 65, no. 3, pp. 2189–2198, Mar. 2018.

[9] M. Lakshmi and S. Hemamalini, "Nonisolated high gain DC-DC converter for DC microgrids," *IEEE Trans. Ind. Electron.*, vol. 65, no. 2, pp. 1205–1212, Feb. 2018.

[10] H. Keyhani and H. A. Toliyat, "Flying-capacitor boost converter," in *Proc. IEEE 27th Annu. Appl. Power Electron. Conf. Expo*., Orlando, FL, USA, 2012, pp. 2311–2318.

[11] U. Manandhar, B. Wang, X. Zhang, G. H. Beng, Y. Liu, and A. Ukil, "Joint control of three-level DC-DC converter interfaced hybrid energy storage system in DC microgrids," *IEEE Trans. Energy Convers.*, vol. 34, no. 4, pp. 2248–2257, Dec. 2019.

[12] K. Jin, M. Yang, X. Ruan, and M. Xu, "Three-level bidirectional converter for fuel-cell/battery hybrid power system," *IEEE Trans. Ind. Electron.*, vol. 57, no. 6, pp. 1976–1986, Jun. 2010.

[13] Y. Shan, J. Hu, Z. Li, and J. M. Guerrero, "A model predictive control for renewable energy based AC microgrids without any PID regulators," *IEEE Trans. Power Electron.*, vol. 33, no. 11, pp. 9122–9126, Nov. 2018.

[14] S. Vazquez *et al.*, "Model predictive control: A review of its applications in power electronics," *IEEE Ind. Electron. Mag.*, vol. 8, no. 1, pp. 16–31, Mar. 2014.

[15] S. Kouro, P. Cortes, R. Vargas, U. Ammann, and J. Rodriguez, "Model predictive control—A simple and powerful method to control power converters," *IEEE Trans. Ind. Electron.*, vol. 56, no. 6, pp. 1826–1838, Jun. 2009.

[16] D. Zhang, C. Chen, Y. Ou, T. Zheng, and W. Tang, "Model predictive control of three-level bidirectional DC-DC converter based on super capacitor energy storage system," in *Proc. Int. Conf. Elect. Eng.*, Istanbul, Turkey, 2020, pp. 1–5.

[17] V. Jayan, A. Ghias, and A. Merabet, "Modeling and control of three-level bi-directional flying capacitor DC–DC converter in DC microgrid," in *Proc. 45th Annu. Conf. IEEE Ind. Electron. Soc.*, Lisbon, Portugal, 2019, pp. 4113–4118.

[18] V. Jayan and A. Ghias, "Operation and control of five-level bi-directional flying capacitor DC-DC converter in DC microgrid," in *Proc. IEEE 4th Int. Future Energy Electron. Conf.*, Singapore, 2019, pp. 1–6.

[19] D. E. Quevedo, R. P. Aguilera, M. A. Perez, P. Cortes, and R. Lizana, "Model predictive control of an AFE rectifier with dynamic references," *IEEE Trans. Power Electron.*, vol. 27, no. 7, pp. 3128–3136, Jul. 2012.

[20] P. Acuna *et al.*, "Sequential phase-shifted model predictive control for a five-level flying capacitor converter," in *Proc. IEEE Int. Conf. Ind. Technol.*, Melbourne, VIC, Australia, 2019, pp. 533–538.

[21] V. Jayan, A. Ghias, and A. Merabet, "Fixed frequency model predictive control of three-level bi-directional flying capacitor DC-DC converter in DC microgrid," in *Proc. 45th Annu. Conf. IEEE Ind. Electron. Soc.*, Lisbon, Portugal, 2019, pp. 3343–3348.

[22] V. Jayan and A. Ghias, "Fixed frequency model predictive control of five-level bi-directional flying capacitor DC-DC converter in DC microgrid," in *Proc. IEEE 4th Int. Future Energy Electron. Conf.*, Singapore, 2019, pp. 1–6.

[23] H. Chen, D. Wang, S. Tang, X. Yin, J. Wang, and Z. J. Shen, "Continuous control set model predictive control for three-level flying capacitor boost converter with constant switching frequency," *IEEE J. Emerg. Sel. Topics Power Electron*., to be published, doi: 10.1109/JESTPE.2020.3044963.

[24] P. Cortes *et al.*, "Guidelines for weighting factors design in model predictive control of power converters and drives," in *Proc. IEEE Int. Conf. Ind. Technol.*, Gippsland, VIC, Australia, 2009, pp. 1–7.

[25] S. Vazquez, J. Rodriguez, M. Rivera, L. G. Franquelo, and M. Norambuena, "Model predictive control for power converters and drives: Advances and trends," *IEEE Trans. Ind. Electron.*, vol. 64, no. 2, pp. 935–947, Feb. 2017.

[26] S. Thielemans, T. J. Vyncke, and J. A. A. Melkebeek, "Weight factor selection for model-based predictive control of a four-level flying capacitor inverter," *IET Power Electron.*, vol. 5, no. 3, pp. 323–333, Mar. 2012.

[27] S. A. Davari, D. A. Khaburi, and R. Kennel, "An improved FCS-MPC algorithm for an induction motor with an imposed optimized weighting factor," *IEEE Trans. Power Electron.*, vol. 27, no. 3, pp. 1540–1551, Mar. 2012.

[28] T. Dragičević and M. Novak, "Weighting factor design in model predictive control of power electronic converters: An artificial neural network approach," *IEEE Trans. Ind. Electron.*, vol. 66, no. 11, pp. 8870–8880, Nov. 2019.

[29] P. Acuña, L. Morán, M. Rivera, R. Aguilera, R. Burgos, and V. G. Agelidis, "A single-objective predictive control method for a multivariable single-phase three-level NPC converter-based active power filter," *IEEE Trans. Ind. Electron.*, vol. 62, no. 7, pp. 4598–4607, Jul. 2015.

[30] M. Norambuena, C. Garcia, J. Rodriguez, and P. Lezana, "Finite control set model predictive control reduced computational cost applied to a flying capacitor converter," in *Proc. 43rd Annu. Conf. IEEE Ind. Electron. Soc.*, Beijing, China, 2017, pp. 4903–4907.

[31] X. Zhang, B. Wang, U. Manandhar, H. B. Gooi, and G. Foo, "A model predictive current controlled bidirectional three-level DC/DC converter for hybrid energy storage system in DC microgrids," *IEEE Trans. Power Electron.*, vol. 34, no. 5, pp. 4025–4030, May 2019.

[32] A. M.Haidekker, "Building blocks of linear systems," in *Linear Feedback Controls*, M. A. Haidekker, Ed., 2nd ed. Amsterdam, The Netherlands: Elsevier, 2020, pp. 219–251.

Vijesh Jayan (Student Member, IEEE) received the B.Tech. degree in electrical and electronics engineering from the National Institute of Technology Puducherry, Karaikal, India, in 2016. He is currently working toward the Ph.D. degree in power engineering with the School of Electrical and Electronic Engineering, Nanyang Technological University, Singapore.

From 2016 to 2018, he was a Technical Trainee with Nuclear Power Division, Lloyd's Register Energy Pvt., Ltd., Mumbai, India. His research interests include power converter topologies, model predictive control, renewable energy systems, and power quality.

Amer Mohammad Yusuf Mohammad Ghias (Senior Member, IEEE) received the B.Sc. degree in electrical engineering from Saint Cloud State University, St Cloud, MN, USA, in 2001, the M.Eng. degree in telecommunications from the University of Limerick, Limerick, Ireland, in 2006, and the Ph.D. degree in electrical engineering from the University of New South Wales (UNSW), Kensington, NSW, Australia, in 2014.

From February 2002 to July 2009, he had held various positions, such as Electrical Engineer, Project Engineer, and Project Manager, while working with the top companies in Kuwait. He was with the UNSW during 2014–2015 and the University of Sharjah, Sharjah, United Arab Emirates, during 2015–2018. In 2018, he joined the Nanyang Technological University as an Assistant Professor. He is also the Cluster Director (Power Electronics and the Energy Management) with Energy Research Institute @ NTU, Singapore. His research interests include model predictive control, hybrid energy storage, renewable energy sources, multiphase drives, new multilevel converters, and advanced modulations for the multilevel converter. Dr. Ghias is an Editor for *IET Power Electronics*.